Ceramics International 51 (2025) 12035–12048

Contents lists available at ScienceDirect

Ceramics International

journal homepage: www.elsevier.com/locate/ceramint

Photocatalytic activity in anatase TiO_2 nanoparticles: Key insights from additive segregation and transition metal oxide doping

Matheus Horstmann Fernandes [a], Bruno Ramos [a,c], Andre Luiz da Silva [a,*], Jefferson Bettini [d], Antonio Carlos Silva Costa Teixeira [b], Douglas Gouvêa [a]

[a] Department of Metallurgical and Materials Engineering, Escola Politécnica, University of São Paulo, Av. Professor Mello Moraes, 2463, 05508-030, São Paulo, Brazil
[b] Department of Chemical Engineering, Escola Politécnica, University of São Paulo, Av. Prof. Luciano Gualberto, 380, 05508-900, São Paulo, Brazil
[c] Department of Chemical Engineering, Centro Universitário FEI, Av. Humberto de Alencar Castelo Branco, 3972, 09850-901, São Bernardo do Campo, Brazil
[d] Brazilian Nanotechnology National Laboratory (LNNano), Rua Giuseppe Maximo Scolfaro 10000, BR-13083100, Campinas, SP, Brazil

ARTICLE INFO

Handling Editor: Dr P. Vincenzini

Keywords:
Anatase
Photocatalysis
Advanced oxidation processes
Dopant segregation

ABSTRACT

This paper focuses on optimizing the photocatalytic performance of anatase TiO_2 nanoparticles by employing two key methodologies: additive segregation and transition metal doping. We investigate the effects of incorporating chromium (Cr), copper (Cu), iron (Fe), and manganese (Mn) into the semiconductor. Using selective dopant lixiviation and X-ray photoelectron spectroscopy (XPS), we confirm the surface segregation of the dopants, which significantly affects the catalytic activity of the nanoparticles. We systematically demonstrate that Cr-doped TiO_2 enhances the catalytic oxidation of acetaminophen compared to pristine TiO_2 and alternative dopants, particularly under low-energy light sources. This enhanced performance is attributed to the segregation of Cr ions on the semiconductor surface. Furthermore, photocatalytic assessments under UV and white light irradiation, along with catalysts subjected to dopant removal via selective lixiviation, consistently demonstrate a return to photocatalytic efficiencies mirroring those of the undoped sample. These findings underscore the major role of surface composition in dictating the photocatalytic capabilities of TiO_2-based photocatalysts.

1. Introduction

Photocatalytic applications of pure and doped TiO_2 have gained significant attention due to their ability to degrade pollutants and organic compounds under UV light irradiation [1,2]. These applications include water purification, air purification, and self-cleaning surfaces [2]. Moreover, developing an efficient and stable TiO_2 photocatalyst is crucial for addressing environmental issues and improving quality of life [1,3,4]. Pure TiO_2 has a wide bandgap, which limits its photocatalytic activity to the UV region. However, doping TiO_2 with different metal or nonmetal elements can modify its bandgap, extend its activity to the visible light range, and reduce charge carrier recombination [5]. Doped TiO_2 photocatalysts have been found to be more effective than pure TiO_2 in degrading pollutants, such as dyes, pesticides, and pharmaceuticals, as well as in bacterial inactivation. The efficiency of photocatalysis can also be enhanced by controlling the morphology and surface area of TiO_2 nanoparticles [1], which can be achieved by selecting dopants or so-called additives prone to interface segregation.

Additive segregation on anatase interfaces occurs when ions preferentially adsorb on the surface or at the grain boundary (solid–solid interface) of anatase TiO_2 nanoparticles [4,6,7]. This phenomenon reduces interface energies, as predicted by Gibbs adsorption theory [8–10]. Additive segregation can also alter the electronic structure and surface acidity/basicity of anatase TiO_2 nanoparticles, significantly affecting their catalytic activity [11–13]. The degree of additive segregation can be controlled by varying the preparation method and conditions, such as the type and concentration of the additive, temperature, pH of the solution, chemical affinity, and the atmosphere during calcination [14–18]. Understanding additive segregation on anatase surfaces is essential for optimizing the performance of anatase TiO_2-based catalysts and for designing new catalysts with improved efficiency and selectivity.

In this study, we selected four transition metal elements, Cr, Cu, Fe, and Mn, and carefully studied their interfacial segregation in TiO_2 nanoparticles and their influence on photocatalytic activity. The segregation of transition metals on the surface of anatase can impact photocatalytic activity by altering the composition of adsorption sites. Furthermore, their ability to be stable between different valence states,

* Corresponding author.
E-mail address: andresilva.urussanga@usp.br (A.L. da Silva).

https://doi.org/10.1016/j.ceramint.2025.01.055
Received 25 June 2024; Received in revised form 16 December 2024; Accepted 4 January 2025
Available online 6 January 2025

facilitated by the stability of electron numbers in the d-shell orbitals, and their capacity to absorb visible light may also contribute to this phenomenon. Importantly, since these metal ions are not expected to participate in the bulk of the material, their influence on the concentration of electronic defects in the energy bands is probably minimal. Studies investigating the effects of additive ions such as Cr, Fe, and Cu on the recombination of electron-hole pairs in anatase have shown that the presence of these ions leads to an increase in the recombination rate. This outcome suggests that the phenomenon must have a different primary cause. In the same study, the authors also observed a shift in the point of zero charge, indicating alterations in surface chemistry [19].

Transition metals have partially filled d-shell orbitals, which can interact with ligands and affect the stability of the oxidation state [20]. It is common for transition metal ions to have multiple oxidation states due to their ability to lose or gain electrons from their partially filled d-shell orbitals. The strength of the metal-ligand bond can modify the energy required to remove or add these electrons and change the oxidation state stability of transition metal cations. The coordination number of these ions can also influence this stability [21–23]. Metal cations with a higher coordination number tend to be more stable because they are surrounded by more ligands, which can better stabilize the oxidation state of these ions. Additionally, this stability can also be affected by the nature of the ligands: a stronger field tends to form more stable products with the metal cation, thereby influencing the stability of its oxidation state. The coordination environment provided by the surface can also affect the stability of the transition metal ion. Due to the low stability on the surface, an increase in the reactivity of transition metal ions is expected. It is evident that the surface properties play a crucial role in determining the variable degrees of oxidation or reduction processes exhibited by each individual metal ion.

The electronic configuration of transition metals, including chromium, copper, manganese, and iron, imparts them with the capability to absorb visible light. The partially filled d-orbitals of these metals allow for electron excitation between distinct energy levels upon absorption of photons with specific wavelengths [21–23]. This interaction can enhance charge transfer during photocatalysis by synergizing with the electronic structure of TiO_2. Through the incorporation of segregated transition metals, along with their specific electronic configurations and the surrounding material, it becomes possible to modify light absorption properties and thereby influence the efficiency of charge transfer during photocatalysis [19,24,25].

The application of the selective lixiviation technique facilitates the targeted removal of segregated ions, allowing for a focused evaluation of their actual impact on the photocatalytic properties of TiO_2 [7,26–28]. This work aims to retain soluble ions in the bulk while exclusively eliminating those segregated on the surface and in direct contact with the solution. The goal of this research is to accurately determine the specific contribution of the dopants by analyzing the photocatalytic activity before and after selective lixiviation.

2. Materials and methods

2.1. Synthesis of undoped and doped TiO_2 nanocatalysts

TiO_2-based catalysts were synthesized using a variation of the polymeric precursor method. In this method, the titanium oxide polymeric precursor was prepared by mixing titanium isopropoxide (19.4 wt % - Sigma–Aldrich, ≥97.0 wt % purity) and ethylene glycol (45.4 wt% - Synth, $C_2H_6O_2$ ≥ 99.0 wt % purity) at 40 °C, increasing the temperature to 70 °C, and adding citric acid (35.2 wt % - Synth, $C_6H_8O_7$, ≥99.0 wt % purity). The resulting solution was then heated to 120 °C for 1 h to promote a polyesterification reaction [29]. Doping was performed using acidic solutions containing the dopant cation at a concentration of 0.2 mol L^{-1}. These solutions were prepared by dissolving the appropriate amount of the cation nitrate in an aqueous nitric solution (0.1 mol L^{-1}), which served as a solubilizing medium. The final cation concentration of 0.2 mol L^{-1} was confirmed by ICP analysis [29]. The cations chosen as dopant additives were Cr, Cu, Fe, and Mn, selected for their ability to exhibit multiple oxidation states. A thermogravimetric analysis of the precursor resin containing Ti ions was performed to ascertain the quantity of TiO_2. The requisite amount of precursor resin was weighed, and acidic solutions of each transition metal ion were incorporated to reach the specified concentration of 1 mol%.

The nanoparticles were obtained by mixing calculated amounts of the polymeric precursor and the dopant solution, targeting a dopant molar concentration of 1.0 %. For the preparation of undoped TiO_2, no dopant solution was added to the polymeric precursor. The calcination was carried out in two steps. First, the samples were held at 350 °C in air for 4 h to decompose the organic matrix of the precursor. Then, the resulting powders were manually ground with a mortar and calcinated again at 350 °C in air for 15 h to promote particle size stabilization and complete the oxidation process [29]. The samples were named according to the dopant transition metal cation and are referred to as TiO_2, TiO_2-Cr, TiO_2-Cu, TiO_2-Fe, and TiO_2-Mn in the remainder of this work.

2.2. Sample characterization

The chemical compositions were analyzed by X-ray fluorescence (XRF) using a Malvern Panalytical Zetium spectrometer. X-ray diffraction patterns were obtained using a Panalytical Empyrean diffractometer with Cu-K_α ($\lambda = 1.5406$ nm) radiation at 0.02° steps per second. Data were collected in the 2θ range of 5–90° and analyzed using Panalytical X'Pert HighScore Plus software. Crystallite sizes were calculated using the Rietveld refinement method with an aluminum-magnesium spinel powder (COD No. 96-900-2165) as a standard. The density of the powders was assessed by gas pycnometry using a Micrometrics AccuPyc II 1340 gas pycnometer after 200 degassing purges. Specific surface areas were measured using the Brunauer-Emmett-Teller (BET) method with nitrogen gas adsorption (77 K) in a Micromeritics Gemini VII system. The samples were prepared by applying a degassing treatment at 300 °C for ~16 h in a Micromeritics VacPrep 061.

2.3. Surface characterization

The surface excess of the cationic dopants in the TiO_2 nanocatalysts was determined using a selective surface lixiviation method [7,26,29], and X-ray photoelectron spectroscopy (XPS) was used to confirm the presence of segregated dopants on the surface. Surface lixiviation was performed by mixing ~100 mg of the powder with 2 g of an acid solution, followed by ultrasonication for 1 h and centrifuging at 13,000 rpm (10,390 G) for 20 min. The acid solution used for the TiO_2-Cu and TiO_2-Mn samples was a 0.1 mol L^{-1} HNO_3 solution (pH = 1), while for the TiO_2-Cr and TiO_2-Fe samples, an aqua regia solution (1:3 M ratio of nitric acid to hydrochloric acid) was used. After centrifugation, approximately 1 g of the supernatant solution was collected, diluted in ~10 g of deionized water, and analyzed by inductively coupled plasma optical emission spectroscopy (ICP–OES) using a Spectro Across spectrometer. The lixiviated powders were washed five times using the same ultrasonication and centrifugation procedure but with distilled water instead of an acid solution. Between each wash, the water was discarded, and the same amount of clean distilled water was added. The lixiviated and washed powders were dried at 70 °C for 24 h. The samples subjected to the lixiviation treatment received the identification prefix "lix" for labeling purposes.

EELS measurements were conducted using a JEM-2100F (JEOL) equipped with an 863 GIF Tridiem spectrometer (Gatan). The measurement was carried out in STEM mode. The probe size used was 0.5 nm, the pixel size for the EELS image spectrum was 0.35 nm, and the pixel acquisition time was 0.25 s. The spectral image was processed with PCA using temDM software [30].

XPS measurements were performed using a UNI-SPECS UHV spectrometer with a pressure of less than 5×10^{-7} Pa. An Al K_α line was used

as the ionizing source, and the pass energy was set to 10 eV. The inelastic noise from the high-resolution spectra was subtracted using Shirley's method. Voigt profiles with a Gaussian (70 %) and Lorentzian (30 %) combination were used to deconvolute the spectra. Peak indexing was performed according to the National Institute of Standards and Technology database with an accuracy of ~0.1 eV.

2.4. UV–VIS and photoluminescence spectroscopy

A Shimadzu UV–VIS–NIR UV-3600i Plus spectrometer was used to measure the reflectance of the photocatalyst powders. The system was equipped with an integrating sphere to correct for light scattering effects during data collection. The reflectance was determined by diffuse reflectance spectroscopy (DRS). A Shimadzu RF-5301 PC spectrofluorometer was used to collect the photoluminescence spectra with an excitation wavelength of 350 nm, an excitation slot of 15 nm, an emission slot of 10 nm, an emission range of 360–700 nm, and step size of 1.0 nm.

2.5. Photocatalysis

The photoactivity of the powders was studied through the degradation of acetaminophen (ACT), also known as paracetamol, which was selected as a model contaminant. ACT was chosen as the test molecule for evaluating catalytic efficiency due to its established use as a standard reaction for quantifying the photocatalytic activity of TiO_2 [31]. This choice minimizes potential interference from UV radiation-induced decomposition or surface adsorption, allowing for an accurate assessment. Furthermore, paracetamol demonstrates well-known and distinct decomposition mechanisms, enhancing the reliability of the experimental results [31]. The tests were performed in a batch reactor containing a suspension with 5 mg of photocatalyst in 4 mL of a 5 ppm aqueous solution of acetaminophen prepared with ultrapure water (18.2 MΩ cm) from a Milli-Q® system (Millipore). A magnetic stir bar was used throughout the analysis to homogenize the suspension. First, the system was kept in the dark for 30 min to establish adsorption-desorption equilibrium. Subsequently, the system was illuminated with LED chips that irradiated the reactor perpendicularly. The LED chips used in this work were a UV LED chip (peak emission at 365 ± 5 nm and irradiance of 4.46 mW cm^{-2}), a white LED chip to simulate white light irradiation (irradiance of 22.7 mW cm^{-2}), and a green LED chip (peak emission at 520 ± 5 nm and irradiance of 21.2 mW cm^{-2}). Aliquots of 0.1 mL were collected at regular intervals, filtered, and diluted in 0.8 mL of deionized water [32]. The concentration of ACT in these solutions was evaluated using a Shimadzu UFLC 20 AD high-performance liquid chromatography system by UV absorbance (243 nm) after separation using a reverse-phase column (Luna C18, 5 μm, 250 × 4.6 mm, Phenomenex Inc.). A mobile phase of methanol: water (1:3) was used at a flow rate of 1.0 mL min^{-1}, with an injection volume of 50 μL and a retention time of ~7 min. These analytical conditions provided ACT detection and quantification limits of 0.08 mg L^{-1} and 0.24 mg L^{-1}, respectively [33]. To improve the interpretation of the data, a simplified kinetic model based on a system of ordinary differential equations (ODE) was used. The model is detailed in Supporting Material 01 (SM01). The code was written in Scientific Python Development Environment (v. 4.1.5, Spyder-IDE.org) using the programming libraries *Numpy* [34], *SciPy* [35], and *lmfit* [36]. The model was solved by minimizing the difference between the simulated and experimental ACT concentrations. The minimization was carried out numerically using the Nelder–Mead method [37]. The ODE system was solved at every minimization step using the LSODA algorithm implemented in the *odeint* function of the library.

3. Results and discussion

3.1. Characterization of the nanoparticles

The analysis of the chemical composition of the samples (Table 1) indicates that the dopant concentrations are all close to the target value of 1 mol%.

Fig. 1 shows the X-ray diffraction patterns of the samples. Peaks marked with a '□' correspond to anatase (COD 96-901-5930), while those marked with a '▽' correspond to rutile (COD 96-900-4143). The TiO_2, TiO_2-Cr, and TiO_2-Cu samples exhibited ~3 % volume fraction of rutile, which is not significant for interpreting the results.

The crystallite sizes of the TiO_2 nanopowders were determined using Rietveld refinement (Table 2). All samples exhibited crystallite sizes in the nanometer range, confirming their nanostructured nature. This nanocrystalline characteristic was further corroborated by the broadened peaks observed in the XRD patterns, as shown in Fig. 1.

The dopants were observed to reduce the average crystallite size of the materials compared to undoped TiO_2. This trend, previously reported for doped TiO_2 [6,7,26,29], is attributed to dopant segregation at interfaces. Such segregation decreases interface energies [10], thermodynamically favoring the formation of nanostructures with smaller dimensions than those produced without dopants. Additionally, interface energies play an important role in the thermodynamics of phase transformations in TiO_2 [9,38] so that changes in these energies can influence the stability of the phases present in the material [4].

According to the theory of phase transformation of nanostructured titanium dioxide, there is a critical particle size above which rutile becomes thermodynamically more stable than anatase [4,9]. In the samples exhibiting both phases, the crystallite size of rutile is larger than that of anatase. This observation suggests that, similar to particle size, a critical crystallite size exists beyond which the transformation from anatase to rutile occurs. The results of this study indicate that this critical crystallite size lies between 21 nm and 27 nm.

The densities of the samples, measured by gas pycnometry with helium, are presented in Table 2. These values deviate from the theoretical density of 3.89 g cm^{-3} for anatase. The undoped sample has the closest density to the theoretical value. In contrast, the doped samples exhibit lower densities than pure TiO_2. Such deviations have also been reported for TiO_2 doped with alkaline-earth metals [6] and are likely related to the presence of defects introduced by the dopants and the nanostructured nature of the materials.

In this study, interfaces were categorized into two groups: solid-solid interfaces, referred to as grain boundaries (GBs), and solid-gas interfaces, or surfaces. The total interfacial area (TIA), which represents the total specific area, was calculated based on the weighted average of anatase and rutile crystallite sizes ($\bar{d}$) and the powder density (ρ) provided in Table 2, as described in Equation (1). The crystallites were modeled as tetrakaidecahedra, an energetically favorable geometric shape [9,39].

$$TIA = \frac{k}{\rho \bar{d}} \qquad \text{Equation 1}$$

Table 1
Chemical composition of the samples prepared to the target dopant concentration of 1 mol%.

Chemical composition (mol%)				
TiO_2	Cr	Cu	Fe	Mn
100.0	–	–	–	–
98.7	1.3	–	–	–
98.9	–	1.1	–	–
98.8	–	–	1.2	–
99.0	–	–	–	1.0

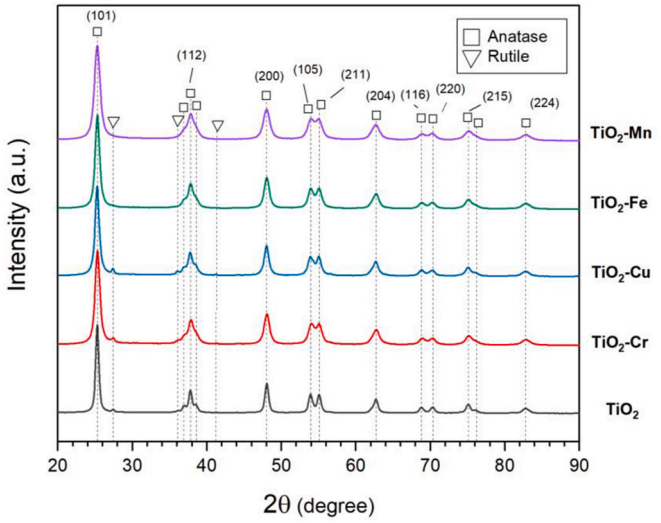

Fig. 1. XRD of TiO_2 and doped TiO_2 prepared at 350 °C for 15 h in air.

Table 2
Crystallite sizes (calculated by Rietveld refinement) and pycnometric density (ρ) of the samples.

Sample	Crystallite sizes (nm)		ρ (g cm^{-3})
	Anatase	Rutile	
TiO_2	21.5 ± 0.3	27 ± 2	3.60 ± 0.01
TiO_2-Cr	12.6 ± 0.1	21 ± 2	3.49 ± 0.01
TiO_2-Cu	15.6 ± 0.2	45 ± 6	3.50 ± 0.01
TiO_2-Fe	13.4 ± 0.1	n.d.	3.50 ± 0.01
TiO_2-Mn	10.1 ± 0.1	n.d.	3.41 ± 0.01

where k is a shape factor derived from the ratio of the surface area to the volume of the geometric shape. For a tetrakaidecahedron, $k = 6.7$.

The specific grain boundary area (SGB) was calculated using Equation (2), with the specific surface areas obtained from gas adsorption (S_{BET}). It was assumed that each grain boundary is shared by two grains and, given the nanometric nature of the material, that one crystallite corresponds to a single grain.

$$SGB = \frac{TIA - S_{BET}}{2} \quad \text{Equation 2}$$

The surface excess (Γ_S) was calculated using the dopant concentration in the solution obtained from the selective lixiviation method, as described by Equation (3), where n_s represents the number of moles of dopant on the surface, determined according to SM02.

$$\Gamma_S = \frac{n_s}{S_{BET}} \quad \text{Equation 3}$$

The results obtained for the total interfacial areas and surface excess are presented in Table 3.

The doped samples exhibit larger specific surface areas (S_{BET}) and specific grain boundary areas (SGB) compared to the undoped sample. This increase is attributed to dopant segregation, which reduces interfacial energy [10,40]. The resulting decrease in interfacial energy enables doped materials to achieve thermodynamic equilibrium with larger specific interfacial areas (surface and/or grain boundaries) than undoped materials [9]. Similar trends of increased interfacial specific areas due to dopant segregation have been reported for TiO_2 doped with alkaline earth metals [6,26,29], niobium oxide [4], and ZnO [7]. Furthermore, the presence of excess surface confirms the occurrence of dopant segregation.

When dopants are introduced into a material, the ratio of grain boundary area to specific surface area may decrease [41] or increase [28], depending on whether the dopants preferentially segregate on the surface or at the grain boundary, respectively. In this study, the SGB/S_{BET} ratio decreased for all compositions, indicating a preference for the dopants to segregate on the surface, leading to a reduction in surface energy and stabilization of this interface. Additionally, surface segregation alters the surface sites, modifying both the surface energy and the chemical composition. These changes are expected to influence the photoactivity of the material. Indeed, the segregation of dopants on the TiO_2 surface plays a critical role in determining its photocatalytic activity, with the chemical composition of the catalyst surface emerging as the primary factor, as demonstrated later.

Surface segregation was also evaluated by STEM EELS elemental mapping, with the TiO_2-Cr sample selected due to the complexity of this measurement. Fig. 2a shows the HAADF image with an orange box highlighting the region where the spectral image was acquired. Fig. 2b, c, and 2d display the peak intensity maps for titanium (red), oxygen (blue), and chromium (green), respectively, while Fig. 2e illustrates the ratio between Cr and Ti peak intensities. The Ti and O maps exhibit contrast variations similar to those in the HAADF image, where thinner regions appear darker across all three images, while the contrast observed in the Cr map is more homogeneous in all images. As shown in Fig. 2e, the Cr-to-Ti ratio indicates chromium enrichment at the nanoparticle edges. For instance, the dark blue region (purple arrow) has an average ratio of 0.05, while the white edge region shows a significantly higher average ratio of 0.39, indicating an 8-fold enrichment of Cr at the edge. These findings suggest the formation of a Cr-enriched surface layer, consistent with the surface excess observed through the selective surface lixiviation method discussed earlier. Similar surface dopant enrichment has been observed in other systems, such as BaO-doped TiO_2 [27], SrO-doped TiO_2, and MgO-doped TiO_2 [26].

3.2. XPS analysis

X-ray photoelectron spectroscopy (XPS) analyses were conducted on pure TiO_2 and TiO_2-Cr samples, selected for their notable photocatalytic performance under UV light irradiation using a monochromatic LED chip, as described in the photoactivity section. Additionally, the lixiviated TiO_2-Cr sample (TiO_2-Cr-lix) was analyzed to assess the removal of surface dopants during the selective lixiviation process.

The high-resolution spectra of the Ti 2p peaks of the pure TiO_2 and TiO_2-Cr samples (Fig. 3) confirm the presence of Cr ions on the surface of the doped samples. Deconvolution revealed components exclusive to the doped samples, corresponding to interactions of Cr cations with titanium and oxygen on the surface.

The high-resolution spectra of the Cr 2p peaks of the TiO_2-Cr and TiO_2-Cr-lix samples (Fig. 4) show that the most abundant Cr cation on the surface is Cr^{3+} (in the form of Cr_2O_3 and $Cr(OH)_3$). Hexavalent

Table 3
Total interface area (TIA), specific grain boundary area (SGB), and surface excess (Γ_S) in TiO_2 nanopowders (% segregated of total additive amount).

Sample	TIA (m^2 g^{-1})	S_{BET} (m^2 g^{-1})	SGB (m^2 g^{-1})	SGB/S_{BET}	Γ_S (μmol m^{-2})	% total segregated
TiO_2	86 ± 3	32.5 ± 0.2	27 ± 3	0.83	–	–
TiO_2-Cr	150 ± 4	76.1 ± 0.4	37 ± 4	0.49	0.297 ± 0.001	13.5 ± 0.1
TiO_2-Cu	116 ± 4	57.9 ± 0.3	29 ± 5	0.50	0.890 ± 0.004	36.9 ± 0.3
TiO_2-Fe	142 ± 2	65.2 ± 0.3	39 ± 2	0.60	0.163 ± 0.001	07.4 ± 0.1
TiO_2-Mn	196 ± 2	86.8 ± 0.4	54 ± 2	0.62	0.272 ± 0.001	18.4 ± 0.1

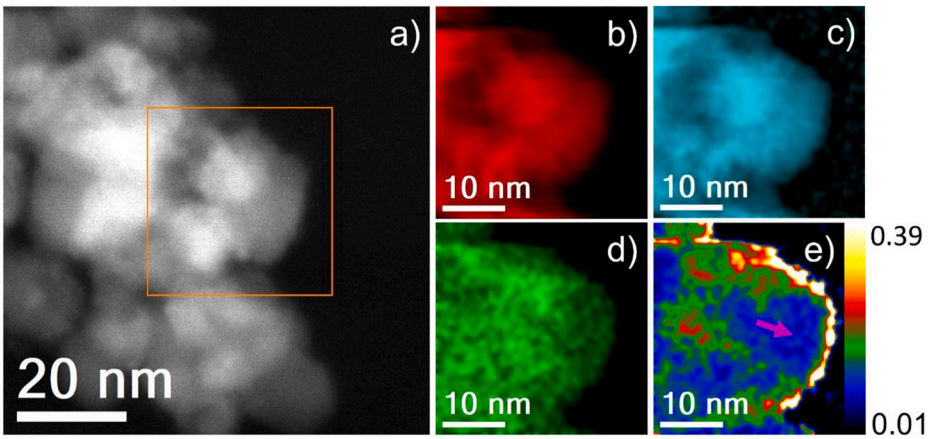

Fig. 2. STEM EELS mapping of the TiO_2-Cr sample. a) HAADF image with an orange box where the spectral image was acquired. b), c), and d) intensity peak maps for titanium (red color), oxygen (blue color), and chromium (green color), respectively; e) ratio between Cr and Ti peak intensities. (For interpretation of the references to color in this figure legend, the reader is referred to the Web version of this article.)

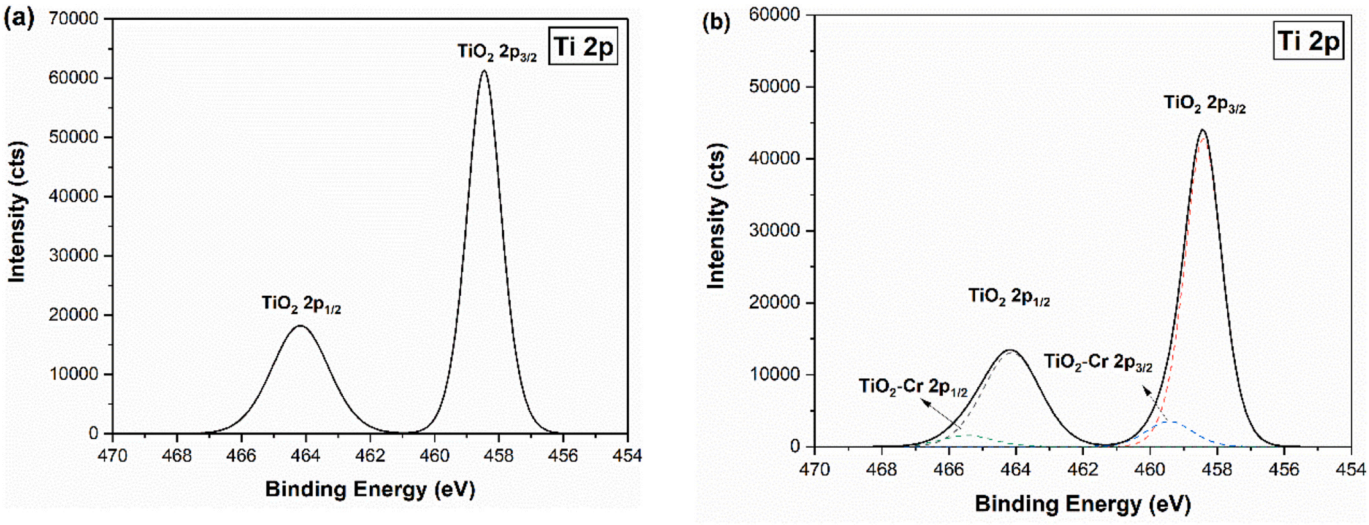

Fig. 3. High-resolution spectra of (a) TiO_2 and (b) TiO-Cr samples.

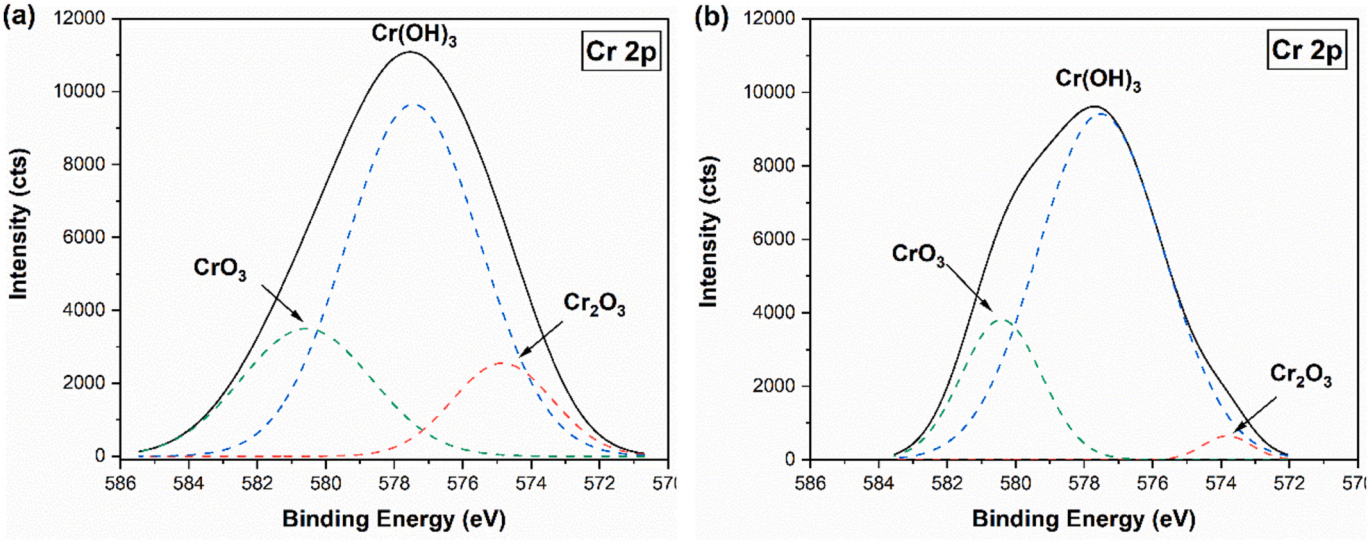

Fig. 4. High-resolution spectra of the Cr 2p peaks from TiO_2-Cr (a) and TiO_2-Cr-lix (b) samples.

chromium cations (in the form of CrO_3) are also present on the surface, as shown by the deconvolution peaks. These results confirm that transition metal cations can exhibit multiple valence states on the surface, supporting their selection as dopants in this study.

The area of the peaks corresponding to Cr^{3+} decreased more significantly than that of Cr^{6+} after leaching, indicating that the lixiviation process preferentially removed trivalent chromium from the surface. Quantitative chemical analysis by XPS was not feasible due to the

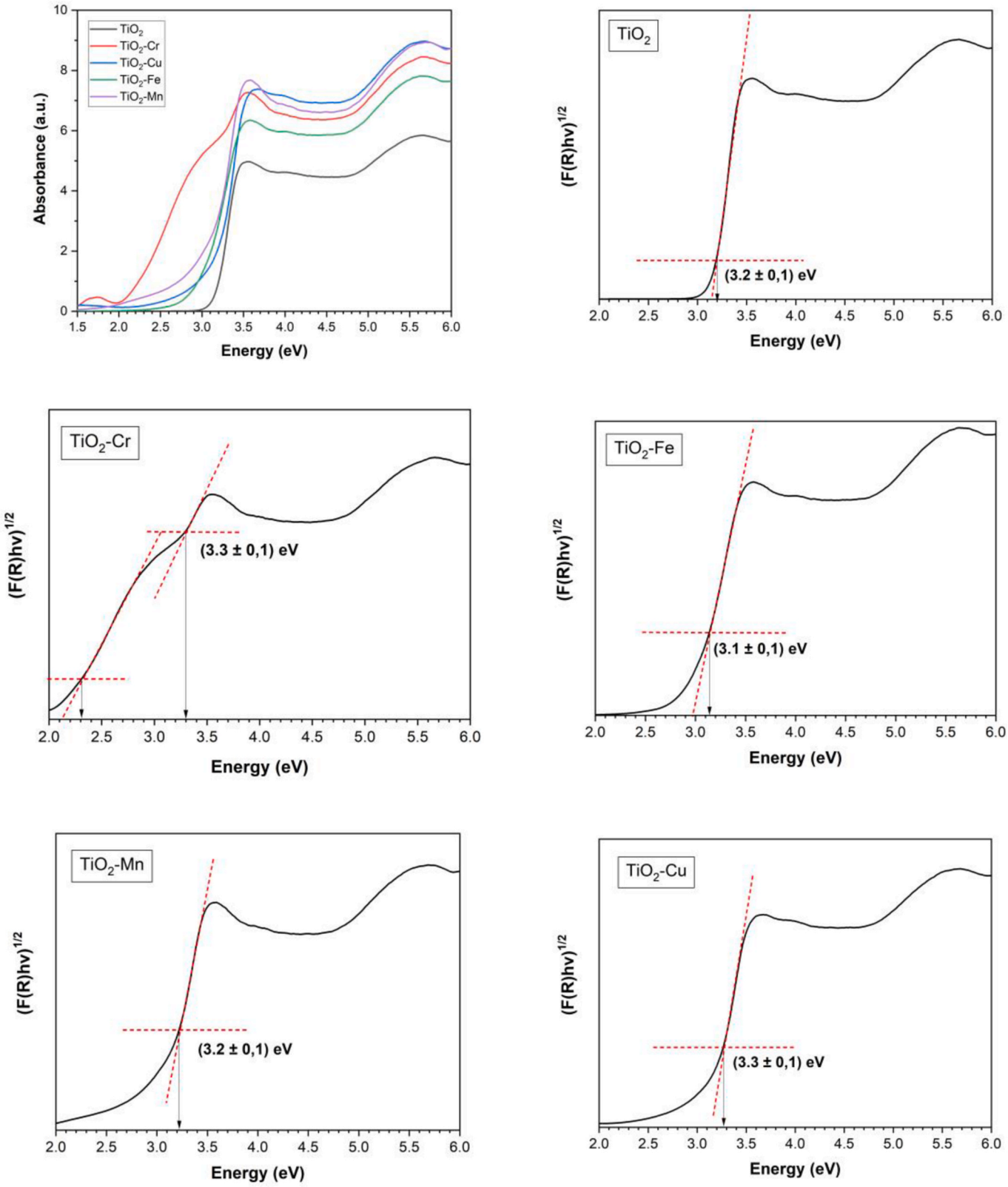

Fig. 5. UV–visible reflectance curves obtained from diffuse reflectance spectroscopy (DRS) along with the Tauc plots of the model incorporating the Kubelka-Munk function applied to TiO_2 nanopowders.

overlap of the Cr 2p peak with the Ti 2s peak and the detection limit of the equipment (~0.5 atoms%) [42]. However, since peak areas are directly proportional to the concentration of the corresponding species [42], a comparison of the Cr 2p peaks before and after lixiviation suggests that approximately 26 % of the chromium ions were removed from the surface during the lixiviation process.

3.3. Bandgap energy estimation

The bandgap energies (E_g) were estimated by applying the Tauc model (TAUC, 1968) to the UV–Visible diffuse reflectance spectra (Fig. 5). This model is described by Equation (4):

$$(\alpha h\nu)^{\frac{1}{\beta}} = (h\nu - E_g) \quad \text{Equation 4}$$

where α is an absorption constant, h is the Planck constant and ν is the frequency of the photon. The variable β depends on the nature of the electronic transitions and is equal to 2 for indirect electronic transitions, as is the case for TiO_2 [43].

The absorption constants (α) were estimated by applying the Kubelka-Munk function [44], described by Equation (5), to the DRS curves (Fig. 5). In this function, R_∞ is the ratio of the sample reflectance to the standard used.

$$\alpha \approx F(R) = \frac{(1 - R_\infty)^2}{2R_\infty} \quad \text{Equation 5}$$

The curves obtained by applying the Tauc model combined with the Kubelka-Munk function (Equation (6)) are shown in Fig. 5.

$$(F(R)h\nu)^{\frac{1}{2}} = (h\nu - E_g) \quad \text{Equation 6}$$

Typically, the energy gap (E_g) is defined as the intersection of the extended linear region of the Tauc curve and the x-axis. However, the presence of defects and dopants can interfere with the discontinuity of the curve associated with the energy gap, potentially leading to a misinterpretation of E_g Ref. [43]. This interference is most prominent in regions corresponding to visible light absorption, as seen in the Tauc curves of the doped samples (Fig. 5). To address this, a correction was applied to the estimation method: E_g was estimated as the intersection between the extension of the linear region of the curve and a baseline drawn at the end of that region [43]. The corrected E_g values are also presented in Fig. 5.

The corrected energy gaps align closely with the commonly reported value for anatase, the predominant phase in the samples, at approximately 3.2 eV [45]. Additionally, the TiO_2-Cr sample exhibited two extra discontinuities in the Tauc curve at (2.1 ± 0.1) eV and (1.3 ± 0.1) eV, as shown in Fig. 5. These features are likely associated with light absorption phenomena caused by electronic transitions within the incomplete d-shell orbitals of the Cr cations.

XPS analysis revealed that Cr^{3+} cations, with an electronic configuration of [Ar]3 d^3, are the most abundant chromium species on the surface of the TiO_2-Cr sample. It is hypothesized that these Cr^{3+} ions form a crystal field on the surface [21–23]. Given the complexity of the atomic bonds present at the surface, this crystal field is assumed to exhibit octahedral symmetry [21–23], which is inherently more intricate than tetrahedral symmetry. Additionally, as Cr^{3+} possesses three unpaired electrons, the resulting crystal field is considered to be weak.

With these considerations in mind, the energies associated with electronic transitions in d-shell orbitals in a crystal field can be estimated using the Orgel [46] and Tanabe-Sugano [47] diagrams for a transition metal with d^3 orbitals in an octahedral crystal field. Both diagrams are provided in SM03. According to these diagrams, the ground state of the electrons, in spectroscopic notation, is $^4A_{2g}$, with three possible transitions. These transitions are represented in spectroscopic notation as:

ν_1: $^4A_{2g} \rightarrow {}^4T_{2g}$

ν_2: $^4A_{2g} \rightarrow {}^4T_{1g}$ (F)

ν_3: $^4A_{2g} \rightarrow {}^4T_{1g}$ (P)

The Tauc curve showed only two absorptions at approximately 1.3 eV ($\nu \sim 10500\ cm^{-1}$) and 2.1 eV ($\nu \sim 17000\ cm^{-1}$). According to the Tanabe-Sugano diagram (T-S diagram), these absorptions could be ν_1 and ν_2 or ν_2 and ν_3. The value of B, a parameter related to the repulsion between the electrons of an atom, was also calculated using the T-S diagram for these two possibilities. The values obtained were 854 cm^{-1} and 270 cm^{-1} for the first and second possibilities, respectively. The value of B for free Cr^{3+} ions is ~845 cm^{-1} [48]. Therefore, the absorptions observed in the Tauc curve were ν_1 and ν_2. From the T-S diagram, the value of the crystal field splitting energy (10Dq) is approximately 10250 cm^{-1}.

The Orgel diagram indicates that the first absorption ν_1 corresponds to 10Dq, as shown in SM03, which is consistent with the initial estimate made by the Tauc curve (~10500 cm^{-1}). The estimated value for ν_2 is also compatible with the calculated value. To confirm the presence of the third absorption in the Tauc curves, the value of ν_3 was calculated considering the Orgel diagram; the value obtained was approximately 26560 cm^{-1}, which corresponds to ~3.3 eV. This energy is close to the 3.2 eV observed in the Tauc curves. Thus, the phenomenon of light absorption at 3.2 ± 0.1 eV could be due to both the transition of an electron from the valence band to the conduction band and electronic transitions within the d-shell orbitals of the dopant cation.

3.4. Photoluminescence

Fig. 6 shows the emission spectra obtained by photoluminescence spectroscopy when exciting the samples with a monochromatic beam with λ = 350 nm. All samples show the same emission peaks at approximately 2.20 eV, 2.62 eV, and 2.78 eV. These peaks represent three different electronic transitions involving intermediate energy levels within the energy gap of the photocatalyst. The observation that doped samples share the same transitions as the undoped sample suggests that doping did not create additional intermediate energy levels. Notably, the emission at 2.20 eV from the TiO_2-Cr sample can also be attributed to the ν_2 transition in the Cr d-shell orbitals in the crystal field, which has the same associated energy.

The relative intensities of the peaks vary among the samples. For instance, samples doped with Cu, Fe, and Mn cations exhibit emission peaks at ~2.20 eV with higher relative intensities compared to the same

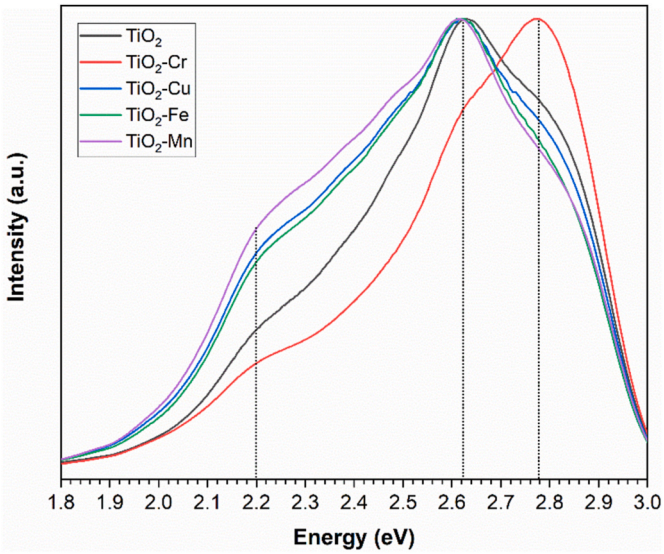

Fig. 6. Emission spectra obtained by photoluminescence spectroscopy.

peak in the undoped material. On the other hand, the sample doped with Cr cations has an emission peak at ~2.78 eV with a higher relative intensity compared to the pure TiO_2 sample. The intensity of an emission peak can be related to the amount of intermediate energy levels involved in the emission process [49]. Thus, while the dopants did not create new intermediate energy levels, their presence influenced the relative quantities of these levels in the samples.

3.5. Photoactivity

Understanding the ability of the catalyst to transfer charges to adsorbed species is crucial in photocatalysis. In this study, acetaminophen was chosen as the reference molecule to evaluate the photocatalytic performance of the materials. Photodegradation of acetaminophen occurs through a sequence of oxidation reactions, typically starting with the transfer of a photogenerated hole from the catalyst to a hydroxyl group adsorbed on the surface, forming •OH radicals that can oxidize acetaminophen [50,51]. However, modifications of the surface chemical composition by cation segregation can alter the natural mechanism. If the surface of the photocatalyst has its composition modified by segregated cations, the reaction mechanism involving the formation of •OH radicals may be different for the doped samples than for the undoped samples, which would directly affect the photocatalytic performance of the material. The charge transfer to the chemical species in aqueous solution is fundamental to the reaction kinetics, and if the bandgap structure is less affected than the chemical composition of the surfaces, the role of segregated species could be determinant for the catalyst performance.

The Langmuir-Hinshelwood kinetic model, which is commonly applied to TiO_2 [52,53], was used to interpret the degradation curves of acetaminophen. Specifically, for low concentrations of the model contaminant (as in this study), the model is expressed according to pseudo-first-order kinetics for a batch reactor, as shown in Equation (7) [53]. This model considers the following assumptions: all reactants are adsorbed and can be desorbed, the intermediate products have a very short lifetime, one of the steps defines the overall reaction rate, and the reactor volume is constant.

$$\ln\left(\frac{C(t)}{C_0}\right) = -k_{ppo}t \qquad \text{Equation 7}$$

where $C(t)$ is the concentration of the organic contaminant at time t, C_0 is its initial concentration (5 ppm for this study), and k_{ppo} is the pseudo-first-order kinetic constant.

For the sake of simplification, the monochromatic UV wavelength LED chip, the white LED chip to simulate white light, and the monochromatic LED chip to simulate green light ($\lambda = 520$ nm) will be referred to as LED-UV, LED-white, and LED-green, respectively, throughout the rest of this study.

3.5.1. Photoactivity - UV

In the photocatalytic tests using LED-UV, all lixiviated and non-lixiviated samples were analyzed (Fig. 7). The kinetic constants for the nonlixiviated (k_{ppo}) and lixiviated (k_{ppo_lix}) samples correspond to the slope of these curves. The values found are represented in Table 4.

The degradation curves show that dopants segregated on the surface are the main factors responsible for the different photocatalytic activities of the doped samples. The doped samples that showed lower photoactivity than the undoped sample (TiO_2-Cu and TiO_2-Mn) had their photocatalytic activity enhanced when dopants were removed from the surface. The Fe cations segregated on the surface, on the other hand, did not cause a significant change in the photocatalytic activity of TiO_2. The photocatalytic performance of the TiO_2-Cr sample, which showed higher photoactivity than the pure TiO_2 sample, worsened after lixiviation of the chromium cations from the surface. The photoactivity of this sample was the closest to that of the undoped sample. As indicated by the XPS results, lixiviation removed approximately 26 % of the dopants segregated on the surface. The remaining dopants on the surface are responsible for the fact that the material still exhibits better photocatalytic performance compared to the undoped sample.

Finally, the possibility that the presence of both rutile and anatase in some samples influenced the photocatalysis results was analyzed. The photocatalysis theory for TiO_2 suggests that the two phases form a heterojunction, thus enhancing the photocatalytic properties of the material [54]. As indicated by the X-ray diffraction results (Fig. 1 and Table 1), the TiO_2, TiO_2-Cr, and TiO_2-Cu samples contained rutile in the same proportion (approximately 3 %). However, the photocatalysis

Table 4
Kinetic constants for acetaminophen degradation using LED-UV.

Sample	k_{ppo}	R^2	k_{ppo_lix}	R^2_{lix}
TiO_2	0.007 ± 0.001	0.998	0.007 ± 0.001	0.996
TiO_2-Cr	0.018 ± 0.001	0.998	0.010 ± 0.001	0.999
TiO_2-Cu	0.003 ± 0.001	0.997	0.007 ± 0.001	0.998
TiO_2-Fe	0.007 ± 0.001	0.998	0.007 ± 0.001	0.999
TiO_2-Mn	0.001 ± 0.001	0.998	0.006 ± 0.001	0.999

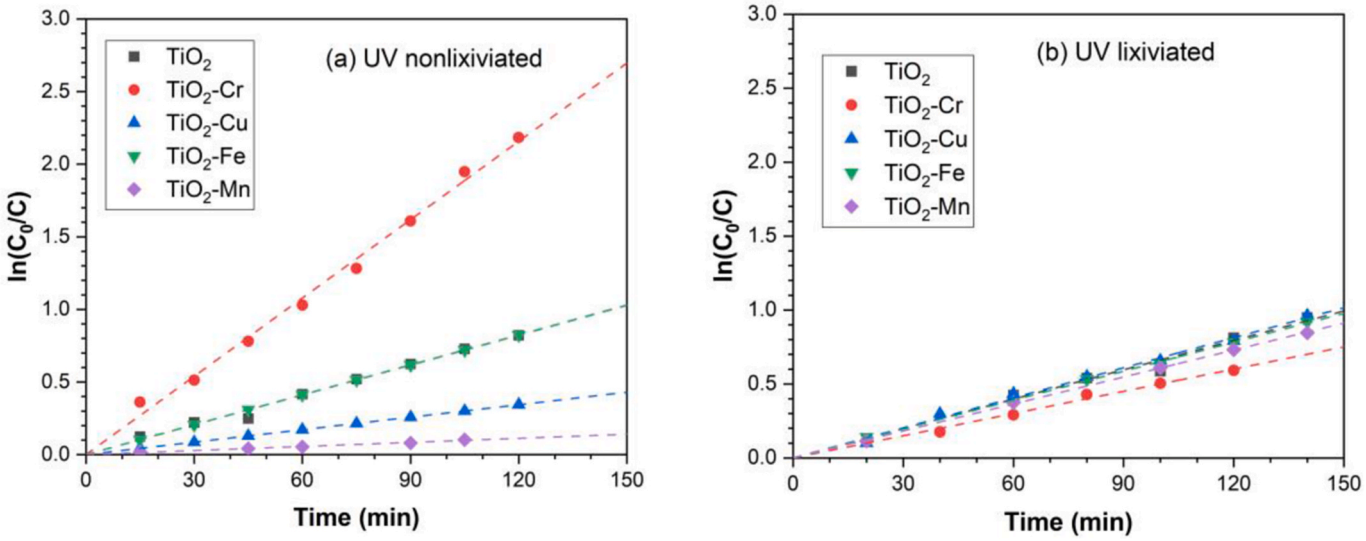

Fig. 7. Pseudo-first-order acetaminophen degradation curves using LED-UV: (a) nonlixiviated samples and (b) lixiviated samples.

results between them were different, which indicates that the presence of the rutile phase did not significantly alter the photocatalytic performance. In addition, if we look at the TiO_2-Fe sample results, which do not have any rutile, we observe that the photocatalytic performance was worse than that of the TiO_2-Cr sample and better than that of the TiO_2-Cu sample. This analysis reinforces that the main agent of photocatalysis is the dopants segregated on the surface of TiO_2.

The transition metals used in this study were selected for their ability to exhibit multiple oxidation states. However, differences in electronegativity among these cations influence their respective capacities for oxidation or reduction.

The photodegradation of acetaminophen is a classical oxidative reaction. Therefore, cations with a higher propensity for hole transfer are expected to demonstrate superior efficiency in facilitating this process. As demonstrated in this study (Section 3.5.5), direct hole transfer occurs when Cr, segregated on the surface, is used as an additive, highlighting its strong oxidative capability. In contrast, materials containing Cu or Mn ions segregated on the surface exhibited lower oxidative performance. Previous studies indicate that Cu-doped TiO_2 and Mn-doped TiO_2 systems are significantly more effective in reduction reactions, which underscores their limited ability to oxidize acetaminophen [55–58].

3.5.2. *Effect of the dopant on the reaction mechanism*

To evaluate the impact of the dopant on the reaction mechanism, a simplified mathematical model (SM01) was developed to investigate the average formation of radicals and holes in the system. The mechanism is based on intermediates commonly found in the photocatalytic oxidation of acetaminophen [31], as pictured in Fig. 8.

The kinetic model (Table S1) assumes that the redox reactions are primarily driven by surface-adsorbed •OH and $^1O_2$, by holes bound to the surface, and by electron transfer in surface-segregated dopant species. It also assumes that the products formed consume •OH radicals with known kinetics and that they can also deactivate the catalyst according to second-order deactivation kinetics. Finally, the quantum yield of electron-hole pair formation (ϕ_{eh}) is estimated from the incoming photon irradiance (E_q) as:

$$\phi_{eh} = \frac{r_{eh} N_A}{E_q} = \frac{r_{eh} c\, N_P\, N_A}{10^{10}\, I\, \lambda} \tag{10}$$

where N_P, N_A, and c refer to Planck and Avogadro constants and the speed of light in vacuum, respectively, all in SI units; I is the irradiance (mW cm^{-2}); λ is the wavelength (nm); and r_{eh} is the kinetics of electron-hole pair generation (mol m^{-2} s^{-1}).

The key results are shown in Fig. 9, and suggest that the catalysts doped with Cu, Fe and Mn exhibit a more reductive behavior, considering the higher concentrations of singlet oxygen available in these systems. Singlet oxygen is formed from the reduction of O_2 molecules adsorbed on the surface, promoted by surface-bound electrons [59]. Conversely, these systems also exhibit the highest degradation rates at the dopant sites but also the highest deactivation kinetics (Fig. 9). This is likely due to the formation of dopant states that act as recombination points, such as CuO, rapidly reducing the number of active sites and hence the degradation kinetics [60], or to the strong adsorption of reaction intermediates to these sites, rendering them inactive. The performance of Fe-doped TiO_2 suggests that the Fe species initially present in the material were converted to less reactive species. This is in agreement with previous experimental observations, where the effect of iron is discussed in terms of the ferric-ferrous redox cycle promoted on the catalyst surface [61]. The quantum yields of all doped catalysts suggest that their incorporation improved charge-carrier separation. However, the concentration of oxidative species (•OH and surface-bound holes) is overall higher in the pure oxide, indicating that the surface- or GB-segregated dopants might act as charge trapping states, impairing the photocatalytic efficiency.

3.5.3. *Photoactivity – white light*

One important effect of the incorporation of metal dopants is the extension of the light absorption edge. To further explore this effect, experiments were carried out with white light and with a longer wavelength source (green light). In the photocatalytic tests using LED-white light, all samples, lixiviated and nonlixiviated, were analyzed. Fig. 10 shows the corresponding acetaminophen degradation curves. The kinetic constants for the nonlixiviated (k_{ppo}) and lixiviated (k_{ppo_lix}) samples correspond to the slope of these curves. The values found are shown in Table 5.

Analyzing the degradation curves of acetaminophen using LED-white, it was found that the photocatalytic performance of all doped samples was superior to that of undoped TiO_2 for both the nonlixiviated and lixiviated samples. Furthermore, as in the LED-UV assays, the difference between the kinetic constants of the doped samples and the

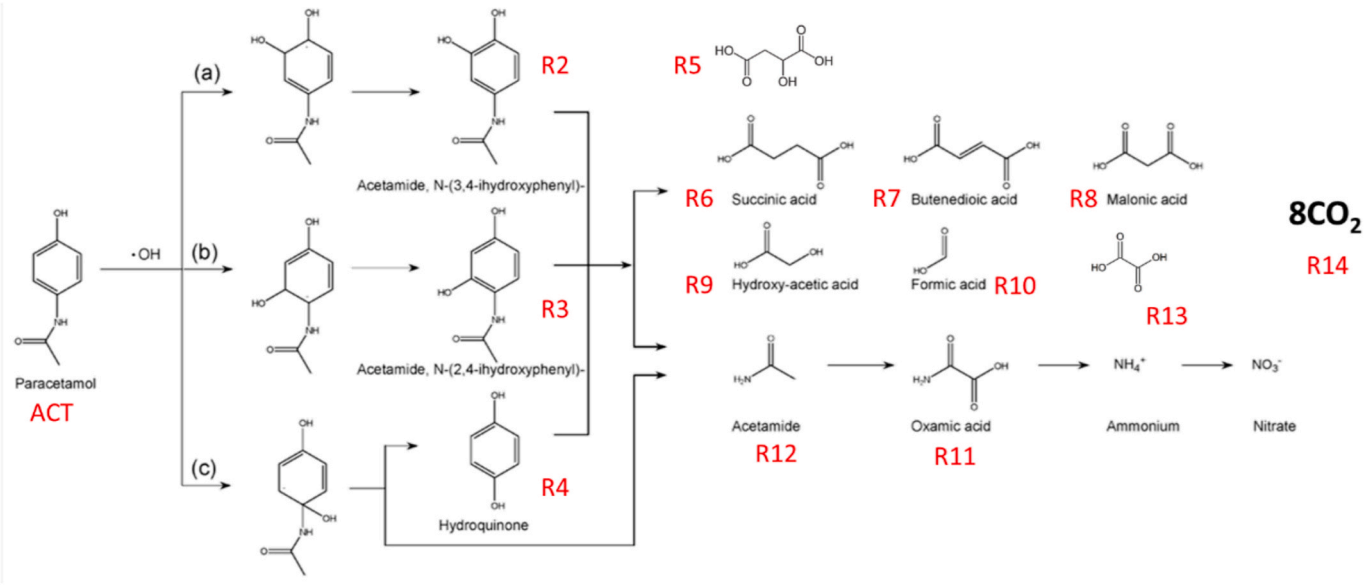

Fig. 8. Intermediates of the photocatalytic oxidation of acetaminophen, with the main chemical species used in the kinetic model designated in red (R1 – R14). Adapted from Ref. [31]. (For interpretation of the references to color in this figure legend, the reader is referred to the Web version of this article.)

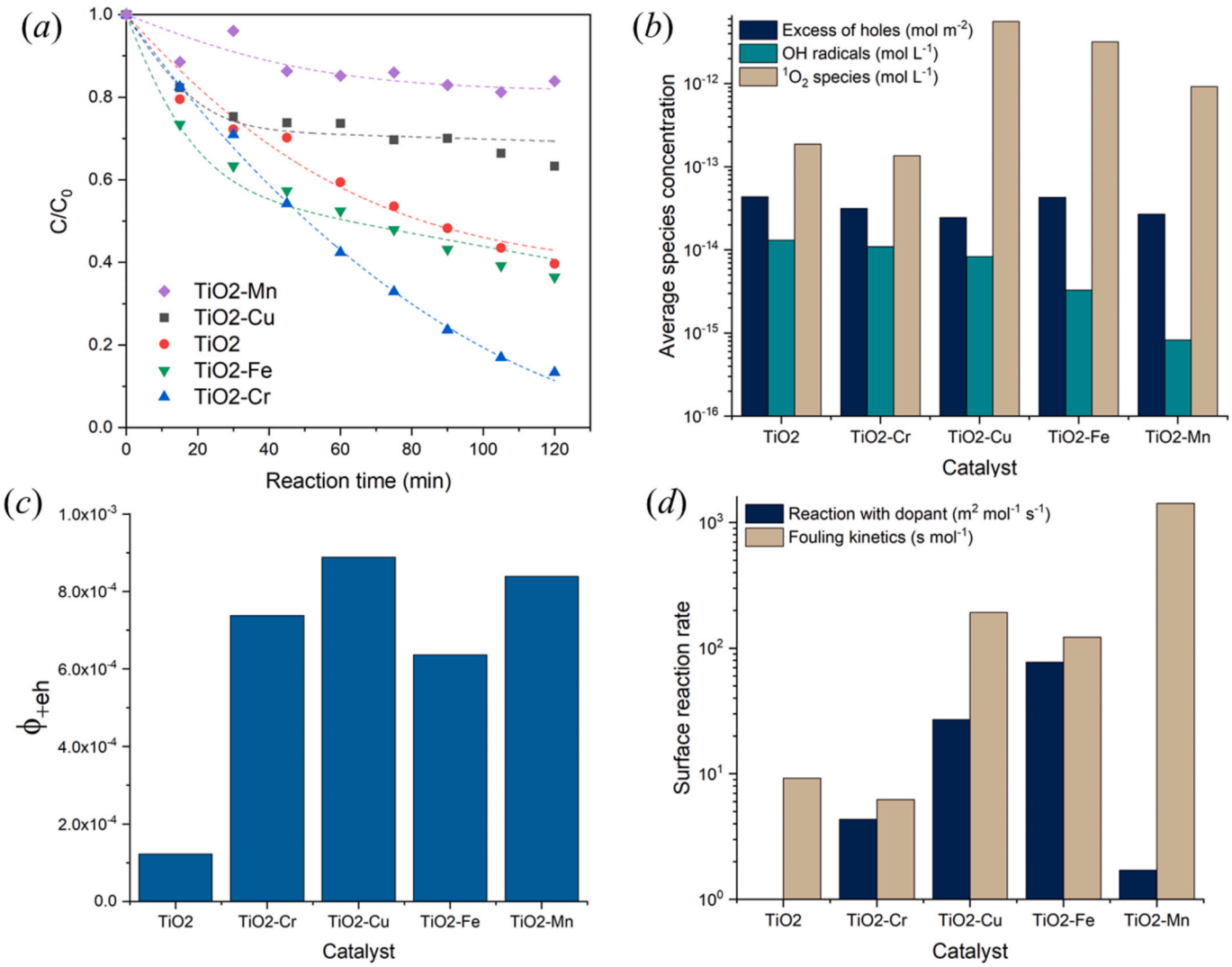

Fig. 9. Effect of dopant on ACT degradation. (a) Reaction kinetics with fitted models (dashed lines). (b) Average concentration of the reactive species. (c) Apparent quantum yield of electron-hole pair formation. (d) Kinetics of surface reactions at dopant sites, direct oxidation and deactivation.

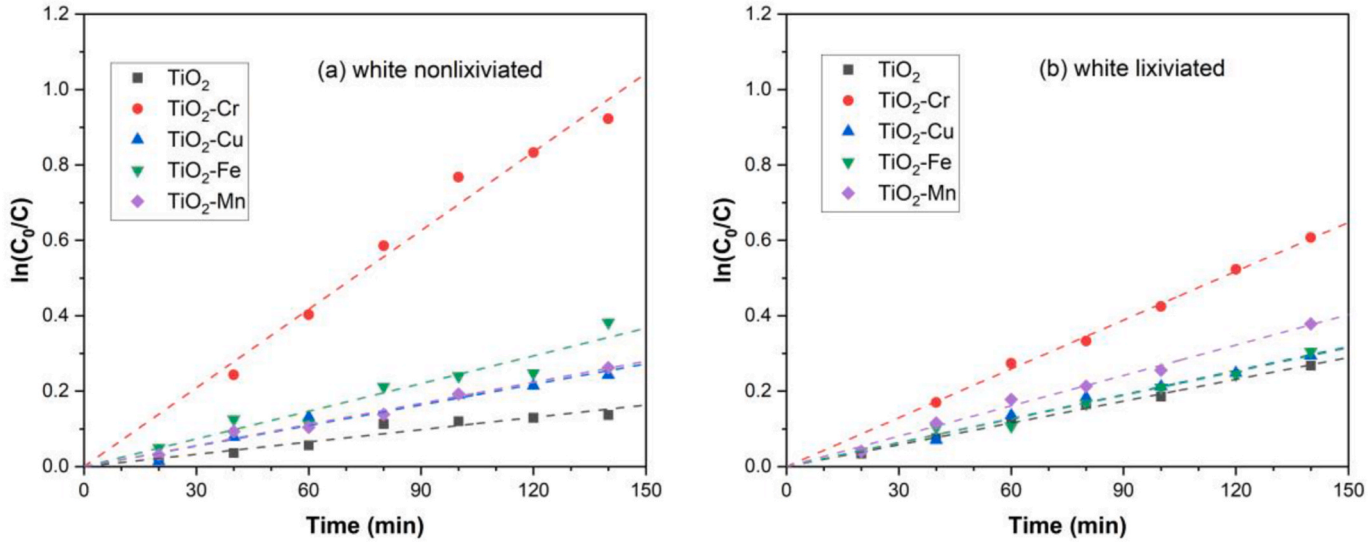

Fig. 10. Pseudo first-order acetaminophen degradation curves using LED-white: (a) nonlixiviated samples and (b) lixiviated samples.

Table 5
Kinetic constants for acetaminophen degradation using LED-white.

Sample	k_{ppo}	R^2	k_{ppo_lix}	R^2_{lix}
TiO_2	0.0011 ± 0.0007	0.991	0.0017 ± 0.0007	0.999
TiO_2-Cr	0.0075 ± 0.0007	0.995	0.0043 ± 0.0007	0.999
TiO_2-Cu	0.0019 ± 0.0007	0.995	0.0021 ± 0.0007	0.998
TiO_2-Fe	0.0026 ± 0.0007	0.995	0.0021 ± 0.0007	0.996
TiO_2-Mn	0.0019 ± 0.0007	0.995	0.0027 ± 0.0007	0.997

undoped sample decreased after lixiviation. This result shows that the dopants segregated on the surface also directly affect photocatalysis when the material is irradiated with white light. The photoactivity of the TiO_2-Cr sample was the least similar to that of the undoped sample, as observed in the LED-UV tests. This fact is related to the chromium cations that remained on the surface even after the lixiviation process.

To better understand the photocatalytic phenomenon, the absorption spectra of nonlixiviated samples obtained by UV–vis diffuse reflectance spectroscopy (solid line in Fig. 11) were compared with the LED-white light spectrum (dashed line in Fig. 11). The comparison shows that all samples doped with transition metal cations exhibit improved absorption of the light emitted by the LED, which corresponds to visible light (~400–750 nm). In particular, the TiO_2-Cr sample exhibits a different behavior compared to the other samples. This results in more efficient light absorption in the visible range compared to the other samples. In the other doped samples, this discontinuity is more pronounced at approximately 400 nm. The TiO_2 sample also exhibits a more pronounced absorption for wavelengths near 400 nm. However, it is noticeable that light absorption starts at wavelengths of approximately 420–430 nm, which corresponds to visible light.

Light absorption in the visible range can occur through mechanisms that do not involve the excitation of electrons from the valence band along the entire energy gap to the conduction band. Such a mechanism is the excitation of electrons from intermediate energy levels to the conduction band. Intermediate levels can be introduced into the energy gap due to the presence of dopants and structural defects. The photoluminescence spectra indicated that the dopants did not induce the formation of new intermediate energy levels in TiO_2. Thus, these levels were attributed to the presence of structural defects (vacancies and interstitials), which may be responsible for the small light absorption observed for undoped TiO_2 in the visible range between 420 and 430 nm.

Therefore, light absorption is a more significant factor for interpreting photocatalytic results compared to LED-UV tests. Photocatalysis using white light has a component related to the chemical composition of the surface and the ability to absorb light.

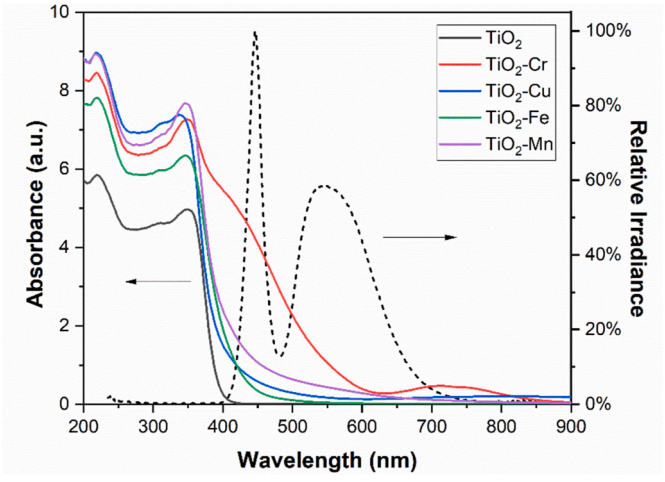

Fig. 11. Comparison between the absorbance of the samples obtained by DRS-UV-white (solid lines) and the spectral output of the LED-white (dashed line).

3.5.4. Photoactivity – green light

To examine the effect of this extended Cr-induced absorption edge, we carried out experiments using irradiation of a longer wavelength (using a green LED). These tests were conducted using only the samples doped with lixiviated and nonlixiviated Cr cations. The choice of an LED chip with a wavelength in the electromagnetic spectrum corresponding to green light was based on the absorbance curve of this sample, shown again in Fig. 12; the light spectra of LED-green and LED-white are also shown in this figure. Fig. 13 shows the degradation curves of acetaminophen by the nonlixiviated and lixiviated samples (TiO_2-Cr-green and TiO_2-Cr-green-lix). The curves obtained for chromium-doped TiO_2, lixiviated (TiO_2-Cr-white-lix) and nonlixiviated (TiO_2-Cr-white) using LED-white are also shown in Fig. 13 for easy comparison of the results.

The degradation curves presented in Fig. 13 show that the photocatalytic activity of Cr-doped TiO_2 using LED-green does not depend on the cations segregated on the surface since the activity was the same for both lixiviated and nonlixiviated samples. Furthermore, it can be observed that the photocatalytic performance of the lixiviated TiO_2-Cr sample under LED-white is similar to that of the lixiviated and nonlixiviated samples when LED-green was used. It was therefore hypothesized that the dopant segregated on the surface absorbs light at different wavelengths than those segregated at the grain boundaries or solubilized in the bulk. This could explain why these three samples have different photocatalytic performances compared to the nonlixiviated TiO_2-Cr sample in tests using LED-white.

An analysis of Fig. 12 reveals that there are two regions of more intense irradiance in the LED-white spectra. One of them, at wavelengths between approximately 500 and 700 nm, is also present for the green LED. The other, located between approximately 400 and 480 nm, only appears for the white LED. Since the photocatalytic performance of the lixiviated TiO_2-Cr-white sample was the same as that of the TiO_2-Cr-green and TiO_2-Cr-green-lixiviated samples, it was hypothesized that the dopant segregated at the grain boundaries and solubilized in the bulk promotes light absorption in the green region. Therefore, the cations segregated on the surface probably promote light absorption in the other main region of the LED-white spectrum (at wavelengths between 400 and 480 nm). This difference in light absorption behavior may be the cause of the different photocatalytic activities observed.

3.5.5. Influence of oxidizing species

Photocatalytic oxidation reactions occur involving oxidizing species

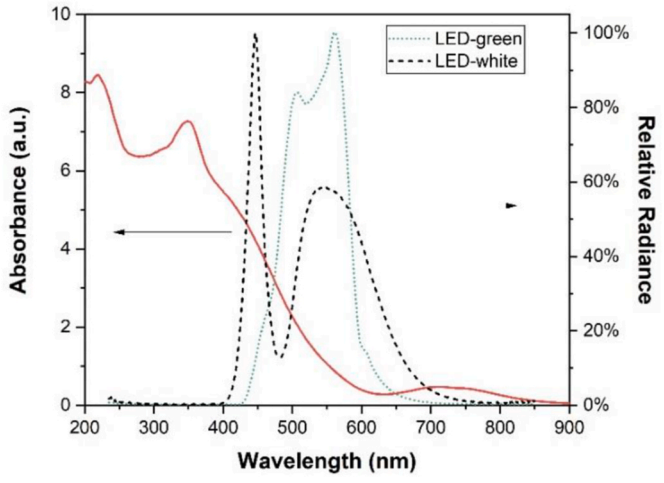

Fig. 12. Comparison between the absorbance of the TiO_2-Cr sample obtained by DRS-UV-white (solid line) and the luminous spectra of LED-white and LED-green (dashed lines). (For interpretation of the references to color in this figure legend, the reader is referred to the Web version of this article.)

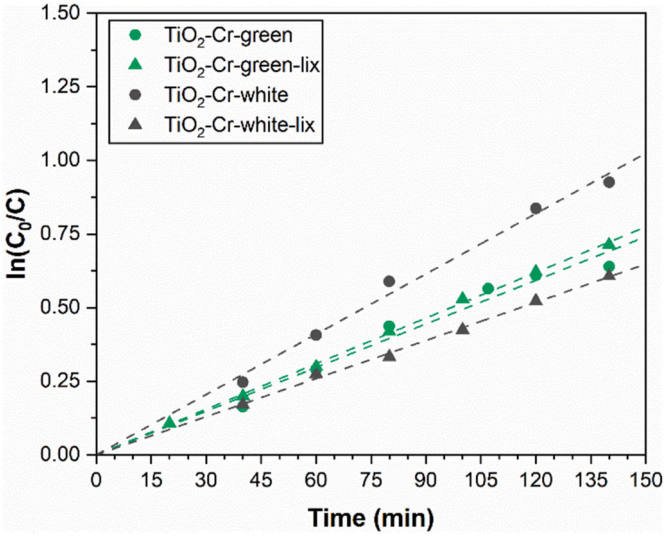

Fig. 13. Comparison of acetaminophen degradation curves for TiO_2-Cr samples with and without luminescence using green and white LEDs. (For interpretation of the references to color in this figure legend, the reader is referred to the Web version of this article.)

formed by the transfer of charge carriers (e^- and h^+) between the photocatalyst surface and species adsorbed on it [33,62]. The most active oxidizing species during these reactions are superoxide radicals ($O_2^{\bullet-}$), hydroxyl radicals ($^{\bullet}OH$), singlet oxygen ($^1O_2$) and holes [33,62]. To analyze the effect of these species on acetaminophen degradation, scavengers were used. To study the action of h^+, $^{\bullet}OH$ and $^1O_2$ species, formic acid (FA), tertiary butyl alcohol (tBu-OH), and sodium azide (NaN_3), respectively, were used [62]. Suppression of superoxide radical and singlet oxygen formation was achieved by bubbling N_2 into the reactor throughout the reaction at a flow rate of 325 mL min^{-1}. The tests were carried out for 60 min under the same conditions as the other photocatalytic tests, using a monochromatic UV LED chip and adding scavengers at a concentration of 0.02 mol L^{-1} to the model contaminant solution (5 mg L^{-1} ACT) [33]. The TiO_2-Cr sample was chosen as the photocatalyst for these tests because it showed the best results for acetaminophen degradation.

Fig. 14 shows that the degradation of ACT in the assay where no scavenger was used was 64.3 % after 60 min of reaction. When

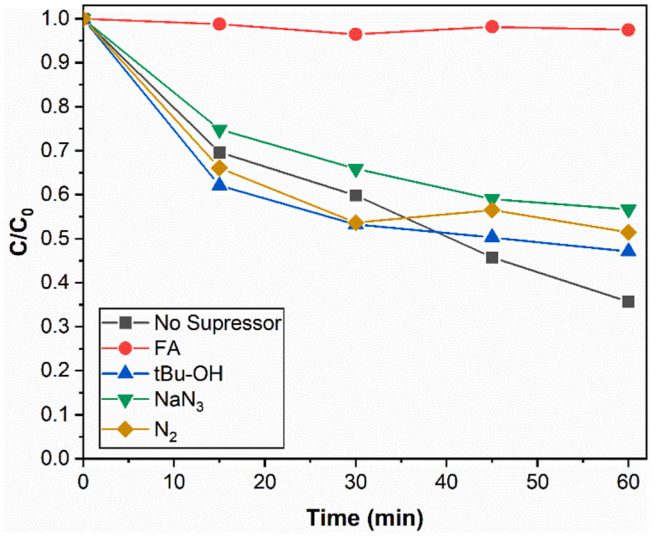

Fig. 14. Effect of scavengers on the photocatalytic UV degradation of acetaminophen ($C_0 = 0.56 \pm 0.01$ mg L^{-1}) by the TiO_2-Cr catalyst.

scavengers of $^{\bullet}OH$ radicals, $O_2^{\bullet-}$ radicals, and $^1O_2$ were used, the degradation of ACT decreased to approximately 43.3 %–52.9 %. This indicates that these three species participate in the photocatalytic process, but the most active oxidizing species are the holes. When the h^+ scavenger was used, only 2.5 % of ACT was removed from the solution.

Since the reaction is governed by the direct oxidation of ACT by holes, it was hypothesized that segregated Cr^{3+} and Cr^{6+} cations on the surface could vary their oxidation states during the reaction, facilitating electron transfer from ACT to holes on the surface. The mechanism by which the reaction would occur would begin with electron transfer from Cr^{3+} to photogenerated h^+ in the VB, with the segregated cations assuming a Cr^{6+} state. The electrons from the ACT molecules would then be transferred to Cr^{6+} cations:

$$TiO_2 \xrightarrow{light} 6e^-_{CB} + 6h^+_{VB}$$

$$2Cr^{3+} + 6h^+_{VB} \rightarrow 2Cr^{6+}$$

$$2Cr^{6+} + 6e^-_{ACT} \rightarrow 2Cr^{3+} + 3ACT_{oxid}$$

Furthermore, the light absorption mechanisms in a crystal field also introduce a new possibility of generating holes in the material through electronic transitions that do not involve the energy gap of the photocatalyst. This ease of generating holes in more than one way may explain why doping with Cr cations allowed an increase in the photocatalytic activity of TiO_2 with respect to ACT degradation.

$$2Cr^{3+} \xrightarrow{light} 2e^-_{exc} + 2h^+$$

$$2e^-_{ACT} + 2h^+ \rightarrow ACT_{oxid}$$

3.6. Efficiency of the photocatalytic process

Finally, a useful parameter for evaluating the efficiency of a photocatalytic process is the electrical energy consumption per order (EE_O) [63], defined as the amount of energy required to reduce the contaminant load by 90 %. Although our catalysts were not tested under optimized reaction conditions, this figure-of-merit provides a common basis for comparing the performance of our materials with other modified TiO_2 materials. The EE_O (kWh L^{-1}) is calculated as:

$$EE_O = \frac{P\,t}{V \log(C_i/C_t)}$$

where P is the electrical power consumed by the light source (kW), t is the batch reaction time (h), V is the reaction volume (L), and C_i and C_t are the initial and final (at time t) concentrations of ACT, respectively. Fig. 15 shows the calculated EE_Os for each material (nonlixiviated) using the different irradiation conditions, along with an average value calculated from a collection of published data for the photocatalytic degradation of ACT with modified TiO_2. Fig. 15b shows the EE_O of our materials in a panorama of other irradiation conditions as a function of the ACT:TiO_2 ratio (mg/g). A complete list of the data and the references are given in the Supplementary Material.

Fig. 15a shows that Cr-doped TiO_2 has the lowest energy demand, approximately 124 kWh L^{-1} under UV-A irradiation, a value approximately 50 % lower than that of undoped TiO_2. The Mn- and Cu-doped catalysts showed worse energetic efficiency (264 % and 93 % increase in energy demand, respectively), while Fe-doped TiO_2 did not show any significant variation in this parameter. Nevertheless, when compared to the average literature values, all materials show a significant improvement (approximately one order of magnitude), likely as a result of the homogeneity and high crystallinity of the nanosized materials obtained by the synthesis and purification procedures. Fig. 15b shows that our materials are overall in the lower half of the EE_O values commonly found for TiO_2-based acetaminophen photodegradation under UV-A irradiation, in particular Cr-doped TiO_2. It should be highlighted that although

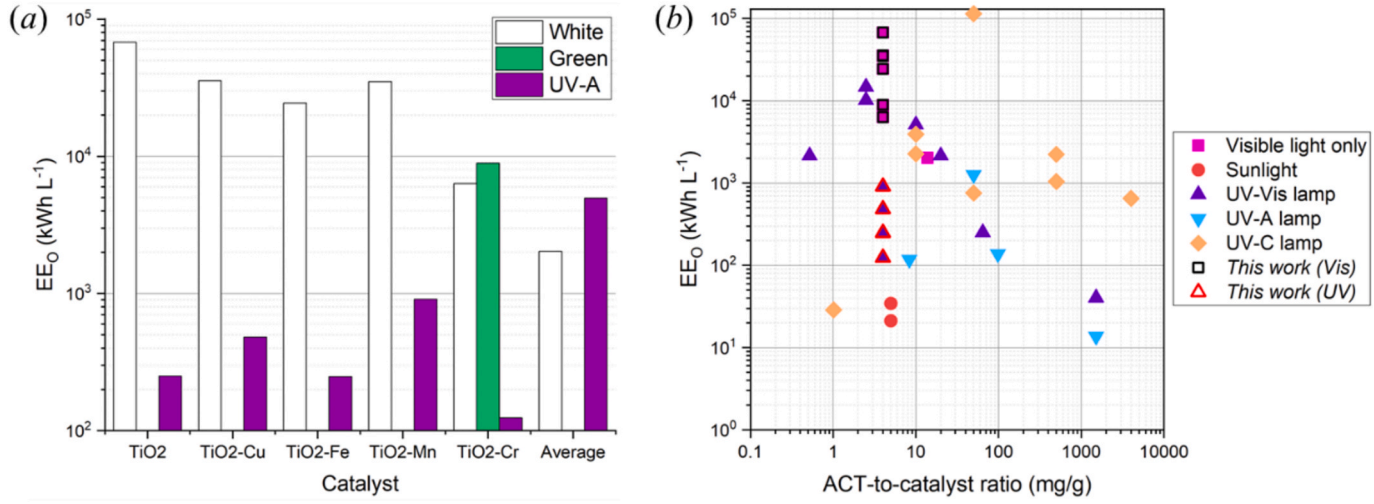

Fig. 15. Electrical energy consumption per order (EE_O). (a) EEO of our modified catalysts for different irradiation conditions and an average calculated from the literature data. (b) Materials reported in this work (□ and △) compared to catalysts reported in the literature (detailed data and references available in the SI).

the EE_O calculated for white light catalysis was higher than that for UV-based processes, their potential for combination with sunlight irradiation is clear. Switching from an artificial to a natural light source significantly reduces the EE_O values, as shown by the position of the sunlight-based processes in Fig. 15b. This indicates that Cr-doped TiO_2 is a viable alternative for the development of sustainable and economical photocatalytic treatments.

4. Conclusion

Titanium dioxide nanoparticles doped with transition metals (Cr, Cu, Fe, and Mn) were evaluated for their photocatalytic activity and interfacial segregation. Transition metals incorporation at approximately 1 mol% was confirmed by chemical analysis. Doping reduced crystallite sizes and increased specific surface areas compared to undoped samples, a trend directly linked to interfacial segregation of dopants, as verified by selective lixiviation. X-ray photoelectron spectroscopy (XPS) analysis of Cr-doped TiO_2 revealed that the predominant surface chromium species was Cr^{3+}. Band gap energy calculations of the doped samples indicated values close to that of pure TiO_2. However, the TiO_2-Cr sample also presented two additional discontinuities in the Tauc curve at (2.1 ± 0.1) eV and (1.3 ± 0.1) eV, which were attributed to the light absorption phenomena arising from electronic transitions within incomplete d-shell orbitals of the Cr cations. The superior photocatalytic performance of Cr-doped TiO_2 emphasized the role of holes as the primary oxidizing species. Furthermore, the combined utilization of the selective lixiviation method and photocatalytic activity assessments highlighted the major role of segregated additives in enhancing photocatalytic efficiency compared to undoped TiO_2. It is expected that this study provides insights into the relationship between dopant segregation and photocatalytic activity, offering guidance for designing more efficient photocatalysts for water treatment and pollutant degradation. Additionally, the methodology developed here could be applied to investigate dopant effects in other semiconductor systems.

CRediT authorship contribution statement

Matheus Horstmann Fernandes: Writing – original draft, Methodology, Investigation, Data curation, Conceptualization. **Bruno Ramos:** Writing – review & editing, Writing – original draft, Validation, Data curation, Conceptualization. **Andre Luiz da Silva:** Writing – review & editing, Writing – original draft, Validation, Formal analysis, Data curation, Conceptualization. **Jefferson Bettini:** Writing – review & editing, Investigation, Data curation. **Antonio Carlos Silva Costa Teixeira:** Writing – review & editing, Writing – original draft, Supervision, Data curation, Conceptualization. **Douglas Gouvêa:** Writing – review & editing, Writing – original draft, Validation, Supervision, Methodology, Funding acquisition, Formal analysis, Data curation, Conceptualization.

Declaration of competing interest

The authors declare that they have no known competing financial interests or personal relationships that could have appeared to influence the work reported in this paper.

Acknowledgments

We gratefully acknowledge the support of the RCGI – Research Centre for Greenhouse Gas Innovation, hosted by the Universidade de São Paulo (USP) and sponsored by FAPESP – São Paulo Research Foundation (grants #2014/50279-4, 2020/15230-5 and 2019/10109-6) and Shell Brasil, and the strategic importance of the support given by ANP (Brazil's National Oil, Natural Gas and Biofuels Agency) through the R&D levy regulation. ACSCT and DG thank the National Council for Scientific and Technological Development (CNPq) (grants #311230/2020-2, #309154/2023-5 and #304712/2021-3, respectively). This research was also supported by LNNano – Brazilian Nanotechnology National Laboratory, CNPEM/MCTIC, TEM proposal n. 20210580.

Appendix A. Supplementary data

Supplementary data to this article can be found online at https://doi.org/10.1016/j.ceramint.2025.01.055.

References

[1] M.T. Noman, M.A. Ashraf, A. Ali, Synthesis and applications of nano-TiO2: a review, Environ. Sci. Pollut. Control Ser. 26 (4) (2019) 3262–3291.
[2] K. Liu, et al., Bio-inspired titanium dioxide materials with special wettability and their applications, Chem. Rev. 114 (19) (2014) 10044–10094.
[3] S. Mustapha, et al., Application of TiO2 and ZnO nanoparticles immobilized on clay in wastewater treatment: a review, Appl. Water Sci. 10 (1) (2020).
[4] A.L. da Silva, D. Hotza, R.H.R. Castro, Surface energy effects on the stability of anatase and rutile nanocrystals: a predictive diagram for Nb2O5-doped-TiO2, Appl. Surf. Sci. 393 (2017) 103–109.
[5] G. Žerjav, et al., Brookite vs. rutile vs. anatase: what's behind their various photocatalytic activities? J. Environ. Chem. Eng. 10 (3) (2022) 107722.
[6] A.L. da Silva, et al., Energetics of CO2 and H2O adsorption on alkaline earth metal doped TiO2, Phys. Chem. Chem. Phys. 22 (27) (2020) 15600–15607.

[7] H. Gandelman, et al., Surface and grain boundary excess of ZnO-doped TiO2 anatase nanopowders, Ceram. Int. 44 (10) (2018) 11390–11396.
[8] J. Nowotny, Science of ceramic interfaces, in: Materials Science Monographs, xx, Elsevier, Amsterdam, the Netherlands ; New York, 1991, p. 612.
[9] R.H.R. Castro, On the thermodynamic stability of nanocrystalline ceramics, Mater. Lett. 96 (2013) 45–56.
[10] R.H.R. Castro, D. Gouvêa, Sintering and nanostability: the thermodynamic perspective, J. Am. Ceram. Soc. 99 (4) (2016) 1105–1121.
[11] A.S. Abouhaswa, Physical properties of anatase TiO2 nanocrystallites: based photoanodes doped with Cr2O3, Opt. Quant. Electron. 52 (3) (2020).
[12] C. Adán, et al., Structure and activity of nanosized iron-doped anatase TiO2 catalysts for phenol photocatalytic degradation, Appl. Catal. B Environ. 72 (1) (2007) 11–17.
[13] S. Naseem, et al., Enhanced photocatalytic activity by tuning of structural and optoelectrical properties of Cr(III) incorporated TiO2 nanoparticles, J. Electron. Mater. 48 (11) (2019) 7203–7215.
[14] Q.-Z. Yan, et al., Sol–gel auto-igniting synthesis and structural property of cerium-doped titanium dioxide nanosized powders, J. Eur. Ceram. Soc. 26 (6) (2006) 915–921.
[15] M.T. Colomer, M.J. Velasco, J.R. Jurado, Synthesis and thermal evolution of TiO2-RuO2 xerogels, J. Sol. Gel Sci. Technol. 39 (3) (2006) 211–222.
[16] J. Escobar, J.A. De los Reyes, T. Viveros, Influence of the synthesis additive on the textural and structural characteristics of Sol−Gel Al2O3−TiO2, Ind. Eng. Chem. Res. 39 (3) (2000) 666–672.
[17] F. Yu, et al., Synergic effect of cation doping and phase composition on the photocatalytic performance of TiO2 under visible light, Catal. Commun. 51 (2014) 46–52.
[18] A.J. Atanacio, T. Bak, J. Nowotny, Niobium segregation in niobium-doped titanium dioxide (rutile), J. Phys. Chem. C 118 (21) (2014) 11174–11185.
[19] A.D. Paola, et al., *Transition metal doped TiO_2: physical properties and photocatalytic behaviour*, Int. J. Photoenergy 3 (2001) 370924.
[20] M. Gerloch, E.C. Constable, Transition Metal Chemistry : the Valence Shell in D-Block Chemistry, Weinheim etc.: VCH, 1994, p. 211. XI.
[21] D. Khomskii, Transition Metal Compounds, Cambridge, United Kingdom: Cambridge University Press. xii, 2014, p. 485.
[22] Y. Jean, Molecular Orbitals of Transition Metal Complexes, Oxford ; New York: Oxford University Press, 2005, p. 275, xii.
[23] I.B. Bersuker, Electronic Structure and Properties of Transition Metal Compounds : Introduction to the Theory, second ed., Wiley. xxxvi, Hoboken, N.J., 2010, p. 759.
[24] R.S. Pavlov, V.B. Marzá, J.B. Carda, Electronic absorption spectroscopy and colour of chromium-doped solids, J. Mater. Chem. 12 (9) (2002) 2825–2832.
[25] R. Janisch, P. Gopal, N.A. Spaldin, Transition metal-doped TiO2 and ZnO—present status of the field, J. Phys. Condens. Matter 17 (27) (2005) R657.
[26] A.L. da Silva, et al., Improving TiO2 anatase nanostability via interface segregation: the role of the ionic radius, J. Phys. Chem. C 127 (3) (2023) 1536–1547.
[27] A.L. da Silva, et al., TiO2 surface engineering to improve nanostability: the role of interface segregation, J. Phys. Chem. C 123 (8) (2019) 4949–4960.
[28] H. Gandelman, et al., Interface excess on Sb-doped TiO2 photocatalysts and its influence on photocatalytic activity, Ceram. Int. 47 (1) (2021) 619–625.
[29] A.L. da Silva, et al., TiO2 surface engineering to improve nanostability: the role of interface segregation, J. Phys. Chem. C 123 (8) (2019) 4949–4960.
[30] P. Potapov, A. Lubk, Extraction of physically meaningful endmembers from STEM spectrum-images combining geometrical and statistical approaches, Micron 145 (2021) 103068.
[31] L. Yang, L.E. Yu, M.B. Ray, Photocatalytic oxidation of paracetamol: dominant reactants, intermediates, and reaction mechanisms, Environ. Sci. Technol. 43 (2) (2009) 460–465.
[32] M.H. Fernandes, et al., Chloride-doped ZnO thin films prepared by spray pyrolysis: effects on microstructural, optical, and photocatalytic properties, Micro Nanostruct. 177 (2023), 207550-207550.
[33] P.H. Palharim, et al., Effect of HCl and HNO3 on the synthesis of pure and silver-based WO3 for improved photocatalytic activity under sunlight, J. Photochem. Photobiol. Chem. 422 (2022), 113550-113550.
[34] C. Harris, et al., Array programming with NumPy, Nature 585 (2020) 357–362.
[35] P. Virtanen, et al., SciPy 1.0: fundamental algorithms for scientific computing in Python, Nat. Methods 17 (3) (2020) 261–272.
[36] M. Newville, et al., Lmfit: Non-linear Least-Square Minimization and Curve-Fitting for Python, vol. 1606, 2016, p. 14, ascl.
[37] J.A. Nelder, R. Mead, A simplex method for function minimization, Comput. J. 7 (4) (1965) 308–313.
[38] H. Zhang, J.F. Banfield, Thermodynamic analysis of phase stability of nanocrystalline titania, J. Mater. Chem. 8 (9) (1998) 2073–2076.
[39] P.R. Rios, M.E. Glicksman, Modeling polycrystals with regular polyhedra, Mater. Res. 9 (2) (2006) 231–236.
[40] C.E. Krill, H. Ehrhardt, R. Birringer, Thermodynamic stabilization of nanocrystallinity, Zeitschrift für Metallkunde 96 (10) (2005) 1134–1141.
[41] G.M. Fortes, et al., Interfacial segregation in Cl−-doped nano-ZnO polycrystalline semiconductors and its effect on electrical properties, Ceram. Int. 47 (17) (2021) 24860–24867.
[42] J.F. Watts, J. Wolstenholme, An Introduction to Surface Analysis by XPS and AES, 1 ed., Chichester, UK: John Wiley & Sons, Ltd., 2003, 224-224.
[43] P. Makuła, M. Pacia, W. Macyk, How to correctly determine the band gap energy of modified semiconductor photocatalysts based on UV–vis spectra, J. Phys. Chem. Lett. 9 (23) (2018) 6814–6817.
[44] P. Kubelka, New contributions to the optics of intensely light-scattering materials. Part I, J. Opt. Soc. Am. 38 (5) (1948) 448–457.
[45] D.A.H. Hanaor, C.C. Sorrell, Review of the anatase to rutile phase transformation, J. Mater. Sci. 46 (4) (2011) 855–874.
[46] C. Housecroft, A.G. Sharpe, d-Block metal chemistry: coordination complexes, in: Inorganic Chemistry, Pearson Education Limited, Harlow, England, 2012, pp. 665–715.
[47] Y. Tanabe, S. Sugano, On the absorption spectra of complex ions II, J. Phys. Soc. Jpn. 9 (5) (1954) 766–779.
[48] M.A. Catalan, F. Rohrlich, A.G. Shenstone, Relations between the low atomic configurations in the long periods, Proceedings of the Royal Society of London. Series A. Mathematical and Physical Sciences 221 (1147) (1954) 421–437.
[49] S. Perkowitz, Optical Characterization of Semiconductors: Infrared, Raman, and Photoluminescence Spectroscopy, 1st ilustr, Michigan: Academic Press, 2012, 220-220.
[50] E. Moctezuma, et al., Photocatalytic degradation of paracetamol: intermediates and total reaction mechanism, J. Hazard Mater. 243 (2012) 130–138.
[51] O. Nasr, et al., Photocatalytic degradation of acetaminophen over Ag, Au and Pt loaded TiO2 using solar light, J. Photochem. Photobiol. Chem. 374 (2019) 185–193.
[52] L. Yang, L.E. Yu, M.B. Ray, Degradation of paracetamol in aqueous solutions by TiO2 photocatalysis, Water Res. 42 (13) (2008) 3480–3488.
[53] J. Borràs-Ferrís, et al., TiO_2 nanostructures for photoelectrocatalytic degradation of acetaminophen, Nanomaterials 9 (4) (2019), 583-583.
[54] Y. Ma, et al., Titanium dioxide-based nanomaterials for photocatalytic fuel generations, Chem. Rev. 114 (19) (2014) 9987–10043.
[55] B. Deng, et al., Enhanced solar conversion of CO2 to CO using Mn-doped TiO2 based on photo-thermochemical cycle, ChemistrySelect 4 (1) (2019) 236–244.
[56] H. Sudrajat, et al., Mn-doped TiO2 photocatalysts: role, chemical identity, and local structure of dopant, J. Phys. Chem. Solid. 144 (2020).
[57] A. Adamu, et al., Investigation of Cu/TiO2 synthesis methods and conditions for CO2 photocatalytic reduction via conversion of bicarbonate/carbonate to formate, J. CO2 Util. 70 (2023) 102428.
[58] K. Bhattacharyya, et al., Selective CO2 photoreduction with Cu-doped TiO2 photocatalyst: delineating the crucial role of Cu-oxidation state and oxygen vacancies, J. Phys. Chem. C 125 (3) (2021) 1793–1810.
[59] A.V. Demyanenko, et al., Singlet oxygen 1O2 in photocatalysis on TiO2. Where does it come from? J. Phys. Chem. C 123 (4) (2019) 2175–2181.
[60] F. Bensouici, et al., Optical, structural and photocatalysis properties of Cu-doped TiO2 thin films, Appl. Surf. Sci. 395 (2017) 110–116.
[61] Z. Li, et al., Effect of Fe-doped TiO2 nanoparticle derived from modified hydrothermal process on the photocatalytic degradation performance on methylene blue, J. Hazard Mater. 155 (3) (2008) 590–594.
[62] J.T. Schneider, et al., Use of scavenger agents in heterogeneous photocatalysis: truths, half-truths, and misinterpretations, Phys. Chem. Chem. Phys. 22 (27) (2020) 15723–15733.
[63] J.R. Bolton, et al., Figures-of-merit for the technical development and application of advanced oxidation technologies for both electric- and solar-driven systems (IUPAC Technical Report), Pure Appl. Chem. 73 (4) (2001) 627–637.